

A Superconducting Single-Atom Phonon Laser

C.A. Potts^{1,†}, W.J.M. Franse¹, V.A.S.V. Bittencourt², A. Metelmann^{2,3,4} and G.A. Steele^{1,*}

¹*Kavli Institute of Nanoscience, Delft University of Technology, PO Box 5046, 2600 GA Delft, The Netherlands*

²*ISIS (UMR 7006), Université de Strasbourg, 67000 Strasbourg, France*

³*Institute for Theory of Condensed Matter, Karlsruhe Institute of Technology, 76131 Karlsruhe, Germany*

⁴*Institute for Quantum Materials and Technology, Karlsruhe Institute of Technology, 76344 Eggenstein-Leopoldshafen, Germany*

[†]Email: c.a.potts@tudelft.nl

^{*}Email: g.a.steele@tudelft.nl

The development of quantum acoustics has enabled the cooling of mechanical objects to their quantum ground state, generation of mechanical Fock-states, and Schrödinger cat states. Such demonstrations have made mechanical resonators attractive candidates for quantum information processing, metrology, and tests of quantum gravity theories. Here, we experimentally demonstrate a direct quantum-acoustic equivalent of a *single-atom laser*. A single superconducting qubit coupled to a high-overtone bulk acoustic resonator is used to drive the onset of phonon lasing. We observe the absence of a sharp lower lasing threshold and characteristic *upper* lasing threshold, unique predictions of single-atom lasing. Lasing of an object with an unprecedented 25 μg mass represents a new regime of laser physics and provides a foundation for integrating phonon lasers with on-chip devices.

INTRODUCTION

The development of the laser in the early 1960s has proven to be one of the most important breakthroughs in modern physics. The laser found its niche in the advancement of atomic physics, resulting in numerous groundbreaking discoveries such as spectroscopic measurements of atomic species^{1,2}, laser cooling of atoms^{3,4}, and the realization of Bose-Einstein condensation^{5,6}. Beyond this, lasers are indispensable tools in areas like gravitational wave detection⁷, biology⁸, chemistry⁹, and even in medicine¹⁰.

The advancements enabled by optical lasers have motivated the development of lasing states of mechanical vibrations — phonon lasers^{11–15}. Coherent sources of phonons are interesting for coupling mechanical strain to electron spins and color centers¹⁶, coherent driving of magnetic spin-waves^{17,18}, improving the resolution of force sensors¹⁹, fundamental tests of quantum mechanics¹⁵, and nonlinear phononics¹⁴. However, to date, phonon lasing has been realized with the center of mass motion of levitated microspheres or ions^{12–15}, limiting the integrability of these coherent phonon sources. In other examples of phonon lasers in literature, the *lasing* state is the result of dispersive or dissipative optomechanical coupling^{16,19–23} — without population inversion — which are well described as mechanical parametric instabilities²⁴ or as optically driven pulsed semiconductor heterostructures^{25–27}.

This article demonstrates, for the first time, the direct phononic analog of a *single-atom* optical laser^{28–30}. A single two-level artificial atom driven coherently into population inversion couples to a bulk on-chip phonon mode generating a lasing state. The lasing is observed through a dramatically extended ringdown of the artificial atom excited by the phonon laser and demonstrates the nearly

threshold-free nature of single-atom lasers. We also observe a unique predicted feature of single-atom lasers, an upper lasing threshold^{29,31,32}. Our experimental observations agree with the theoretical and numerical models we use to characterize the system. Moreover, the bulk nature of the phonon mode may allow the future integration of color centers or quantum dots, enabling strain engineering or coherent mechanical driving. The coherent state generated via phonon lasing may be used as an efficient displacement pulse for generating large dis-

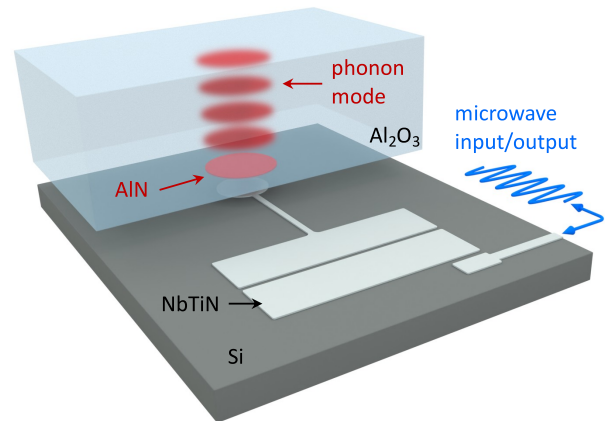


FIG. 1. **Schematic of the on-chip \hbar BAR device.** (A) Rendering of the \hbar BAR device. The \hbar BAR device comprises two chips bounded in a flip-chip orientation. The top chip is 650 μm of sapphire, hosts the HBAR modes (red) and is coupled to the superconducting antenna using an aluminum nitride pad (red). The pocket-style transmon qubit (silver) is fabricated from NbTiN on the bottom silicon chip and coupled to the feedline via an on-chip readout resonator (blue).

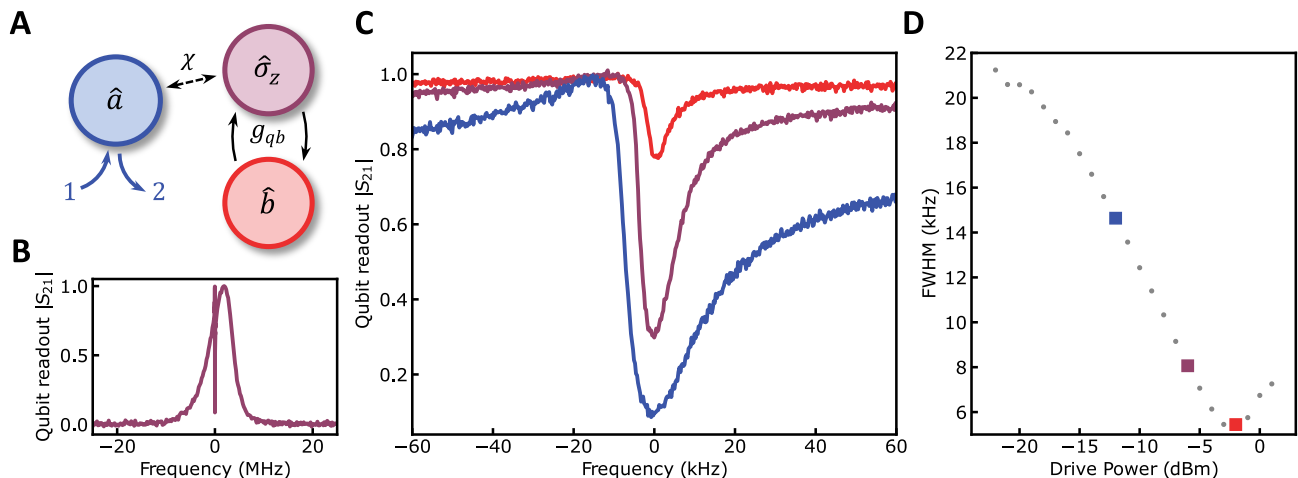


FIG. 2. **Qubit-induced acoustic linewidth narrowing.** (A) Definition of modes and the coupling rates between the modes. The readout resonator \hat{a} has input-output modes labelled 1 and 2. (B) Measured two-tone spectroscopy for drive power of -12.0 dBm set at room temperature. (C) Measured phonon-induced transparency window as a function of qubit drive power. Starting from the lowest curve, drive powers are -12.0, -6.0, and -2.0 dBm set at room temperature, respectively. With increasing power, two features can be noticed. The transparency window reduces in depth, and the full-width half-maximum linewidth narrows. (D) Extracted experimental full-width half-maximum of the transparency window as a function of qubit drive power. Colored points match the corresponding curves in (C).

placement Schrodinger cat states³³. Generating larger cat states may allow for future tests of exotic theories of gravitationally induced quantum decoherence^{34,35}. Future implementations of this architecture may even enable *phonon* spectroscopy of vibrational transitions of complex molecules and crystal structures³⁶ or even biological samples³⁷.

EXPERIMENTAL SETUP

Our device comprises a flip-chip \hbar BAR architecture with two bonded device chips^{33,38–41}. We have implemented a fully on-chip integration, which can multiplex different devices on a single silicon chip^{42,43}. A single feedline is coupled to the individual superconducting fixed-frequency transmon qubits. The transmon qubits were fabricated from niobium-titanium nitride for the bulk structures with aluminum Josephson junctions. A sapphire substrate, 650 μm thick, was positioned above each transmon qubit and bonded to the silicon substrate, see Fig. 1. The sapphire chip supports a set of longitudinal high-overtone bulk acoustic wave resonances (HBARs) separated by a free spectral range of 8.54 MHz. The electric field of a transmon qubit coherently couples to the strain of an HBAR acoustic mode via a disk of piezoelectric aluminum nitride patterned on the sapphire. Each qubit on the chip is nearly resonant with an HBAR mode of interest; in such a way, a pair of qubit-HBAR modes behaves like a single atom coupled to a phononic mode. The qubits were read out via on-chip microwave resonators using standard circuit quantum electrodynamics techniques^{44,45}. Our device is similar to those used in previous work generating mechanical Schrödinger cat states³³ and for circuit quantum acoustodynamics⁴¹.

Using the dispersive shift of a coupled linear readout resonator, we can measure the steady-state qubit population⁴⁴. In the limit where the qubit and the readout resonator are far detuned in frequency, the qubit-cavity Hamiltonian can be written as:

$$\hat{\mathcal{H}}/\hbar = \omega_r \hat{a}^\dagger \hat{a} + \frac{1}{2} \omega_q \hat{\sigma}_z + \chi \hat{\sigma}_z \hat{a}^\dagger \hat{a}, \quad (1)$$

where $\omega_{r,q}$ are the readout and qubit frequency, $\hat{a}^{(\dagger)}$ is the photon annihilation (creation) operator, $\hat{\sigma}_z$ is the qubit population operator, and χ is the qubit-state dependent frequency shift of the readout resonator. The coupling between the phonon and the qubit is described by a resonant Jaynes-Cummings interaction⁴¹, given by the Hamiltonian:

$$\hat{\mathcal{H}}_{\text{int}}/\hbar = g_{qb}(\hat{\sigma}_+ \hat{b} + \hat{\sigma}_- \hat{b}^\dagger), \quad (2)$$

where g_{qb} is the coupling rate between the qubit and the phonon mode, $\hat{\sigma}_\pm$ are the qubit raising and lowering operators, and $\hat{b}^{(\dagger)}$ is the phonon annihilation (creation) operator; see Fig. 2(a).

The qubit's state was measured by applying a weak probe tone on resonance with the readout resonator and monitoring the transmitted signal as a second tone was swept near the qubit frequency. The transmission spectrum at the readout frequency directly maps to the qubit occupation $\langle \hat{\sigma}_z \rangle$; see Fig. 2(b). The asymmetry of the qubit spectrum is due to the finite photon population within the readout resonator^{46,47} and is well described by our theoretical model. Moreover, the narrow transparency window within the qubit spectrum results from the coherent swaps between the qubit and the phonon mode. In this work, the qubit and the phonon frequency

were detuned by approximately 3.3 MHz. See the discussion in the supplementary text for full details. However, as will be discussed below, coherent Rabi oscillations between the qubit and phonon modes do not provide a clear picture of the dynamics at high drive powers.

PHONON LASING

Three distinct features can be observed within the two-tone spectrum when increasing the qubit drive power. First, the qubit linewidth is power-broadened^{46,48}. Large qubit drive powers increase the qubit decay rate due to increased stimulated emission. Less intuitive is the gradual disappearance and narrowing of the phonon-induced transparency window; see Fig. 2(c). The total linewidth of the transparency window is proportional to the phonon linewidth and demonstrates an inverse dependence on the drive power; see Fig. 2(d). This dependence is reminiscent of linewidth narrowing described by the Schawlow-Townes equation and is a known property of lasing states⁴⁹. These features can be understood by considering the schematic shown in Fig. 3(a).

As described before, the qubit and phonon modes coherently exchange excitations at the lowest qubit drive powers, which can be understood as a bosonic beam-splitter-type interaction. However, as the qubit drive power increases, the qubit is excited by the drive and coherently exchanges an excitation with the phonon mode. But before the phonon mode can exchange the excitation back to the qubit, the external drive re-excites the qubit. The qubit excitation can again be coherently swapped into the phonon mode, causing the phonon mode to climb the Fock state ladder. In the steady state, this process results in a phonon mode described by a large coherent state; i.e. the phonon mode starts lasing. A strong qubit drive allows the phonon mode to accept energy from the qubit but prevents the qubit from accepting energy from the phonon mode; see Fig. 3(a). This process also provides an intuitive understanding of the reduced visibility of the transparency window. As the drive power increases, the phonon mode no longer exchanges energy with the qubit; therefore, probing the qubit provides no information about the phonon mode.

Finally, at the highest qubit drive powers, the qubit linewidth has been increased such that the rapid decay of the qubit population results in a *self-quenching* of phonon lasing³¹. Counterintuitively this results in an *upper* lasing threshold above which the phonon mode is no longer lasing. Instead, the qubit incoherently exchanges excitations with the phonon mode, reducing the phonon amplitude. It should also be noted that the phonon mode statistics are no longer described as a coherent state above the upper threshold. This process has been described previously in the context of single-atom photon lasers²⁸ and is captured by our theoretical description; see the supplementary text.

GATED TWO-TONE SPECTROSCOPY

Directly probing the phonon mode is not possible in

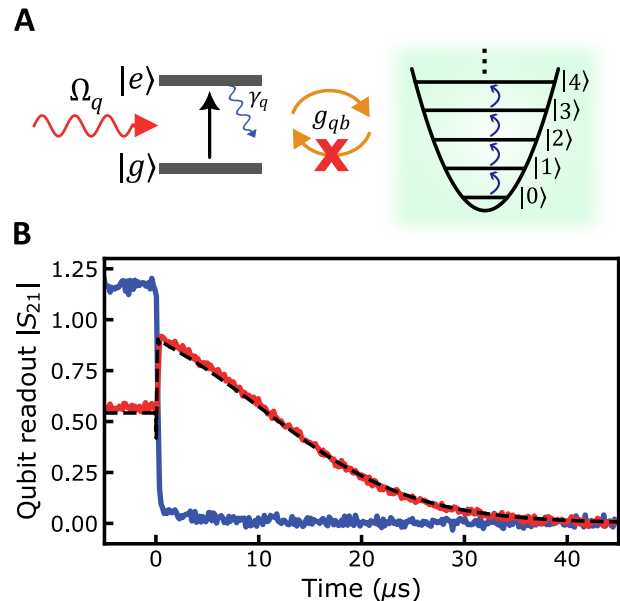


FIG. 3. Phonon lasing observed through qubit ring-down dynamics. (A) Schematic of the coupled qubit-phonon system. The qubit acts as an artificial two-level atom, with ground state $|g\rangle$ and excited state $|e\rangle$. A coherent drive of strength Ω_q drives the qubit between its ground and excited state. The qubit coherently interacts with the phonon mode at a rate g_{qb} . The qubit is rapidly re-excited for strong pump powers, resulting in a one-directional energy flow into the phonon mode. This process results in phonon lasing. (B) Measured qubit ringdown for a qubit drive of -3.0 dBm. Blue line: the qubit drive is detuned from the HBAR by 250 kHz with the phonon mode in the non-lasing state, decaying on a time scale of the ~ 200 ns decay of the qubit. Red line: The qubit drive is tuned directly on resonance with the HBAR mode, exciting it into the lasing state, exhibiting a dramatically longer, non-exponential decay due to re-excitation from the coherently excited phonon mode. The master equation simulation (dashed black line) is plotted over the data.

the current experimental configuration since the readout is performed via the two-level system and not through a propagating photon mode^{14,15}. Direct measurements of the Rabi oscillations between the qubit and phonon state could be possible and have been previously used to measure Fock-states in \hbar BAR devices⁴⁰. However, this data would provide little clarity due to the short lifetime of our qubit and the multiplicity of simultaneous Rabi oscillation frequencies given by $2g_N = 2\sqrt{N}g_{qb}$, which scale with the phonon mode amplitude N .⁴⁰ Instead, we rely on the mismatch between the decay rate of the phonon mode $\tau \sim 25 \mu\text{s}$ and that of the qubit. Using gated two-tone ringdown measurements, we can distinguish pure qubit decay from qubit decay driven by a highly excited phonon state. If the phonon mode is highly excited—in the absence of an external drive—the coherent Jaynes-Cummings interaction will continually drive the qubit, resulting in an extended relaxation of the qubit popula-

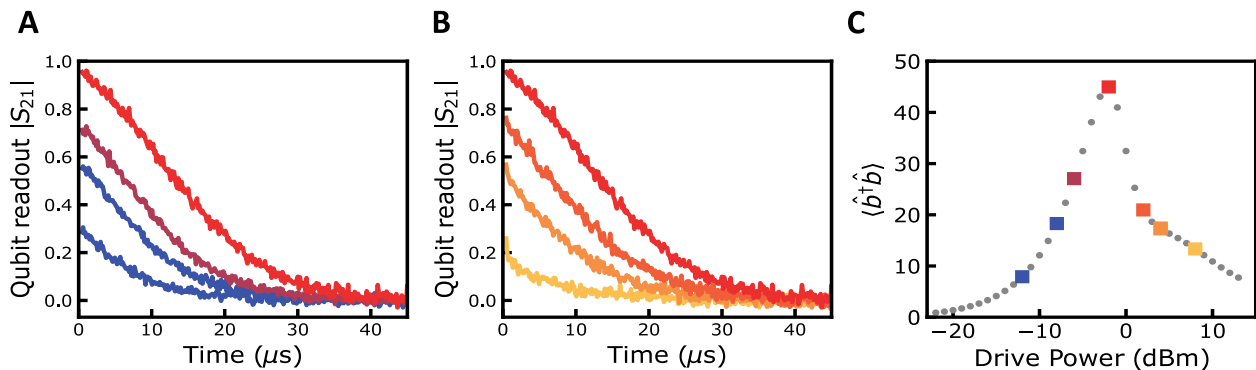


FIG. 4. **Unique signatures of single-atom lasing.** (A) Measured gated qubit ringdown for a qubit drive of -12.0, -8.0, -6.0 and -2.0 dBm. With increasing drive power, the gated qubit ringdowns increase in amplitude and duration as the phonon mode population increases. (B) Measured gated qubit ringdown for a qubit drive of -2.0, 2.0, 4.0, and 8.0 dBm. For all measurements, the qubit drive is tuned directly on resonance with the HBAR mode. With increasing drive power, the gated qubit ringdowns decrease in amplitude and duration as the phonon mode population decreases above the self-quenching threshold. For all measurements in (A) and (B), the qubit drive is tuned directly on resonance with the HBAR mode. (C) Simulated phonon state population $\langle \hat{b}^\dagger \hat{b} \rangle$ as a function of qubit drive power. The phonon population is maximum at a drive power of approximately -2.0 dBm and decreases for drive powers above the upper lasing threshold. The individual trace colors in (A) and (B) correspond to the matching colors within the phonon population plot.

tion compared to its intrinsic relaxation rate.

Gated two-tone measurements were performed, driving the qubit until the system reached its steady state; at this point, the drive was switched off using an RF switch. During the entire sequence, the frequency of the readout resonator is monitored using a vector network analyzer, averaging multiple traces triggered synchronously with the RF switch; see the supplementary text for more information. This measures the expectation value of the qubit population $\langle \hat{\sigma}_z \rangle$ as a function of time, with a temporal resolution of 50 ns.

First, the drive power was set near the peak of the lasing amplitude and was detuned 250 kHz above the HBAR resonance. The gated two-tone measurement was performed, and the blue data points in Fig. 3(b) show the resulting time domain measurement and a ringdown on the order of ~ 200 ns. This corresponds to the intrinsic T_1 decay of the transmon qubit. A second measurement was performed at the same drive power, but the drive was tuned resonant with the HBAR. A ringdown on the order of 25 μs is observed for this configuration, represented by the red data points in Fig. 3(b). The extended ringdown confirms the highly excited phonon amplitude of the mechanical state. When the qubit drive is switched off, the phonon mode can exchange excitations with the qubit, continually re-exciting the qubit until the phonon mode has decayed back to its ground state. Moreover, near the peak phonon amplitude, in contrast to a thermal state, the coherent state generated by the lasing results in a qubit ringdown that is *not* exponential; instead, the qubit ringdown is approximately linear. This feature is captured by our numerical model, the dashed curve in Fig. 3(b). Moreover, our model also captures the ring-up of the qubit and is described within the supplementary

information.

We can estimate the phonon population from our numerical model by fitting the spectroscopic and ringdown data. The estimated phonon population is shown in Fig. 4(c) as a function of qubit drive power. At a power of -2.0 dBm, the phonon population is nearly maximized, corresponding to the ringdown in Fig. 4(a,b), and the upper lasing threshold is clearly visible as the phonon population rapidly reduces with increasing drive power. The upper threshold is experimentally confirmed by performing a set of gated ringdown measurements at a series of qubit drive powers. With increasing qubit drive power, the individual ringdown traces grow in amplitude and increase in duration, corresponding to the increasing phonon population, as shown in Fig. 4(a). At a drive power of -2.0 dBm, the phonon ringdown obtains its peak amplitude and duration, indicating a peak in the phonon population, shown in Fig. 4, which agrees with the minimum in the transparency window linewidth, shown in Fig. 2(b). Further increasing the qubit drive power beyond -2.0 dBm the qubit ringdown decreases in amplitude and duration, a direct indication of the self-quenching nature of the single-atom phonon laser, see Fig. 4(b). The upper threshold is a defining signature of a single-atom laser³¹, and the agreement between the gated qubit ringdown and our numerical simulations indicates that we have indeed demonstrated a single-atom phonon laser.

CONCLUSION

This article demonstrates the experimental realization of a phononic analog to the optical single-atom laser. Our experiment consists of a superconducting single-atom, realized using a transmon style qubit coupled resonantly to an HBAR mode. When driving on resonance with

the HBAR mode, the intrinsic non-linearity of the qubit-phonon coupling generates a highly excited phonon state — the phonon laser. A key feature of this experiment is the population inversion of a two-level atom rather than the parametric instability driving phonon excitations. Moreover, the phonon mode is confined in a bulk longitudinal mode within a sapphire substrate. The bulk nature may allow the phonon laser’s integration with additional on-chip architectures, such as color centers or quantum dots.

Our results have demonstrated the successful generation of a coherent phonon laser, and we have further demonstrated a counterintuitive feature of phonon lasers, an upper instead of a lower lasing threshold³². The size of the coherent lasing state achieved in this work was limited by both the qubit and phonon linewidth. However, the primary limiting factor was the phonon linewidth. Decreasing the decay rates will reduce the upper lasing threshold power and increase the peak lasing amplitude. Future studies could include a linear probe of the phonon mode to probe the phonon statistics. Such an on-chip phonon laser promises to provide a highly coherent source of phonons, which have applications from sensing to quantum information processing.

ACKNOWLEDGMENTS

The authors thank Enrique Sahagun for the device rendering⁵⁰. W.J.M.F and G.A.S. acknowledge support through the QUAKE project, project number 680.92.18.04, of the research programme Natuurkunde Vrije Programma’s of the Dutch Research Council (NWO). C.A.P. acknowledges the support of the Natural Sciences and Engineering Research Council of Canada (NSERC). A.M and V.A.S.V.B. acknowledge financial support from the Contrat Triennal 2021-2023 Strasbourg Capitale Europeenne.

Authors contributions C.A.P. performed experiments, theoretical modelling, conceptualization, and wrote the manuscript. W.J.M.F. fabricated the device and performed experiments. V.A.S.V.B. performed theoretical modelling. A.M. provided supervision and funding acquisition. G.A.S. provided supervision, conceptualization and funding acquisition. **Competing interests:** The authors declare no competing interests.

Data and materials availability All data, analysis code, and measurement software are available in the manuscript or the supplementary material or are available at Zenodo.

Supplementary Information

I. MATERIALS AND METHODS

A. Device Fabrication

Qubit Chip

The device fabrication starts with a 10x10mm chip 525 μm thick high resistivity $\langle 100 \rangle$ silicon deposited with 100 nm of niobium-titanium nitride (NbTiN). The NbTiN film was deposited by the Dutch Institute for Space Research (SRON) following the process described in⁵¹. A layer of photoresist (AR-P 6200.18, 4000 rpm) was patterned, exposed (EBPG 5200, 315 $\mu\text{m}/\text{cm}^2$) and developed (Pentylacetate, O-xylene, IPA) to form the bulk circuitry (transmon islands and coplanar waveguides). The exposed NbTiN was removed using a reactive ion etch (Sentech Etchlab 200, 13.5 sccm SF_6 + 5 sccm O_2 , 55 W, 10 μbar) followed by an in-situ oxygen descum (50 sccm O_2 , 100 W, 10 μbar). After stripping the photoresist, a bilayer resist stack (MAA 8.5% EL6, 2000 rpm and PMMA A6 950k, 1500 rpm; baked for three and five minutes at 180 $^\circ\text{C}$, respectively) was used for patterning the Josephson junctions (190 nm width). The junctions were patterned using e-beam lithography. The bilayer was developed using Cold H_2O : IPA (1:3) and cleaned afterwards with IPA. After cleaning the exposed silicon surface with an oxygen descum (200 sccm, 100 W) and acid clean ($\text{BoE}(7:1):\text{H}_2\text{O}$, 1:1), the chip was placed in an aluminum evaporator (Plassys MEB550). Double-angle shadow evaporation with intermediate in-situ oxidation was used to create Manhattan-style junctions. The aluminum was evaporated at a 35 $^\circ$ angle relative to the substrate at a rotational angle of 0 $^\circ$ and 90 $^\circ$. The top and bottom electrodes were 35 and 75 nm thick, respectively. After the first evaporation step, the aluminum was oxidized to create the AlO_x tunnel barriers. Following the second evaporation step, a second oxidation step was performed to cap the junctions with a passivation layer. After performing liftoff in NMP, the qubit chip was finished.

HBAR Chip

The HBAR chip started with double-side polished four-inch sapphire wafers with a 1 μm thick film of c-axis oriented AlN (Kyma technologies, AT.U.100.1000.B). The wafer was diced into 10x10mm chips for easier processing. A photoresist layer (AR-N 4450.10, 6000 rpm) was used to pattern circular regions, 250 μm in diameter, to mask the

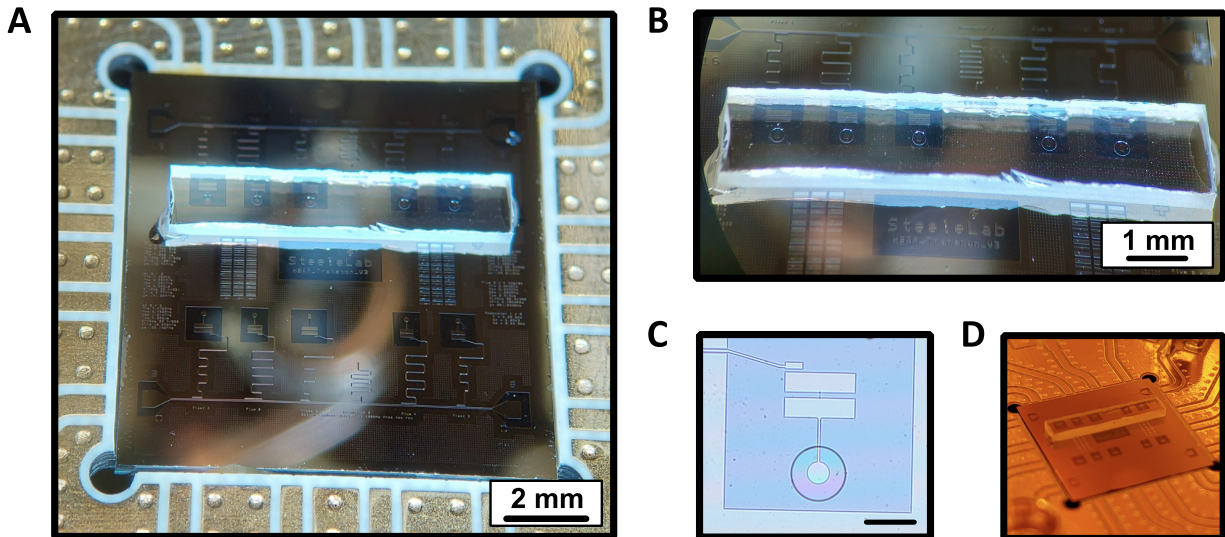


FIG. S1. **Fabricated flip-chip HBAR Device.** (A) Optical micrograph of the assembled flip-chip device. The top feedline of qubits is fabricated with a flip-chip of sapphire, and the bottom feedline has no sapphire flip-chip as references. (B) Zoomed optical micrograph of the flip-chip assembly. (C) Optical micrograph of the qubit with the sapphire chip assembled on top. The overlap between the antenna and the 250 μm aluminum nitride piezoelectric transducer is visible. The scale bar is 250 μm . (D) Optical micrograph of the entire chip loaded in the printed circuit board.

AlN. A reactive ion etch in an Oxford 100 was performed to create AlN disks ($\text{Cl}_2/\text{BCl}_3/\text{Ar}$ at 4.0/26.0/10.0 sccm, 350 W ICP power, 70 W RF power). Following the reactive ion etch, the AlN layer has the proper shape but not the correct thickness. After stripping the photoresist, the chip was placed again inside the etcher to etch the AlN to ~ 900 nm thickness.

Flip Chip

Once fabrication on both chips was done, the HBAR chip was diced into 8x2 mm chips. The HBAR chip was then flipped on top of the qubit chip with the AlN layer facing down. Using probe needles, the AlN disks were aligned with the transmon antennas. Once aligned, the probe needles held down the chips in position while a tapered fiber was used to apply two-component epoxy (Loctite EA 3430) on the sides of the top chip; see Fig. S1. After the epoxy was cured, the chip was wire-bonded and installed onto the baseplate of the dilution refrigerator.

B. Measurement Setup

Two-Tone Spectroscopy

All measurements were performed within a dilution refrigerator operating at a base temperature $T \sim 20$ mK. A schematic of the dilution refrigerator setup and the room-temperature electronics are shown in Fig. S2. The device was mounted on the mixing chamber plate of the dilution refrigerator and connected to a set of coaxial cables. The device was measured in transmission, with the resonators coupled in a 'notch'-style geometry. The output signals went into a cryogenic HEMT (High Electron Mobility Transistor) amplifier (LNF-LNC4-8A), followed by additional room-temperature amplification (Miteq AFS3-04000800-07-10P-4). The input line was attenuated at each stage to reduce the electron temperature and the thermal radiation at the input port of our device. A total of 48 dB of attenuation was used, plus any additional attenuation from the coaxial cables.

The two-tone spectroscopy was measured using a vector network analyzer (VNA). Port one and port three were combined using a directional coupler, with port three attached to the -20 dB coupling port. Port one was set into zero span mode and output a constant signal tuned on resonance with the Stark shifted readout resonator, ω_r , with an output power of -25 dBm. An additional 60 dB of attenuation was added to this signal before the directional coupler. Port 3 was used as a spectroscopic tone and was swept near the qubit frequency, and its power was varied throughout the experiment and had an additional 40 dB of attenuation. The combined signals from port one and three were then connected to the input line of the dilution refrigerator.

The output from the dilution refrigerator was directly connected to port 4 of the VNA set in zero span mode at the readout resonator frequency ω_r . Two-tone spectroscopy was performed by slowly sweeping the qubit drive tone, ensuring the system has reached its steady state and monitoring the readout resonators transmission spectrum S_{21} .

Gated Two-Tone Spectroscopy

For the gated two-tone measurement, port one of the VNA was set up just as in the two-tone measurement. An external signal generator generated the qubit drive tone. The qubit drive tone was passed through an RF switch before being combined with the readout tone using a directional coupler. The RF switch was triggered using a pulse generator at a 3 kHz repetition rate. The signal generator was set to a 22.5% duty cycle, so the qubit drive was off for 75 μs per trace. The VNA was synchronously triggered by the signal generator allowing for 65536 trace averages to be performed (maximum setting). Each trace averaged measurement was repeated 75 additional times to improve the signal-to-noise ratio further.

II. THEORY

A. System Hamiltonian and Master Equation

The system consists of a microwave cavity coupled to a transmon qubit which in turn is coupled to an HBAR phonon mode. The transmon qubit can be considered, up to a good approximation, to be a two-level system. The readout cavity is driven with two coherent tones: one at a frequency ω_p , which we call the probe tone, and one at a

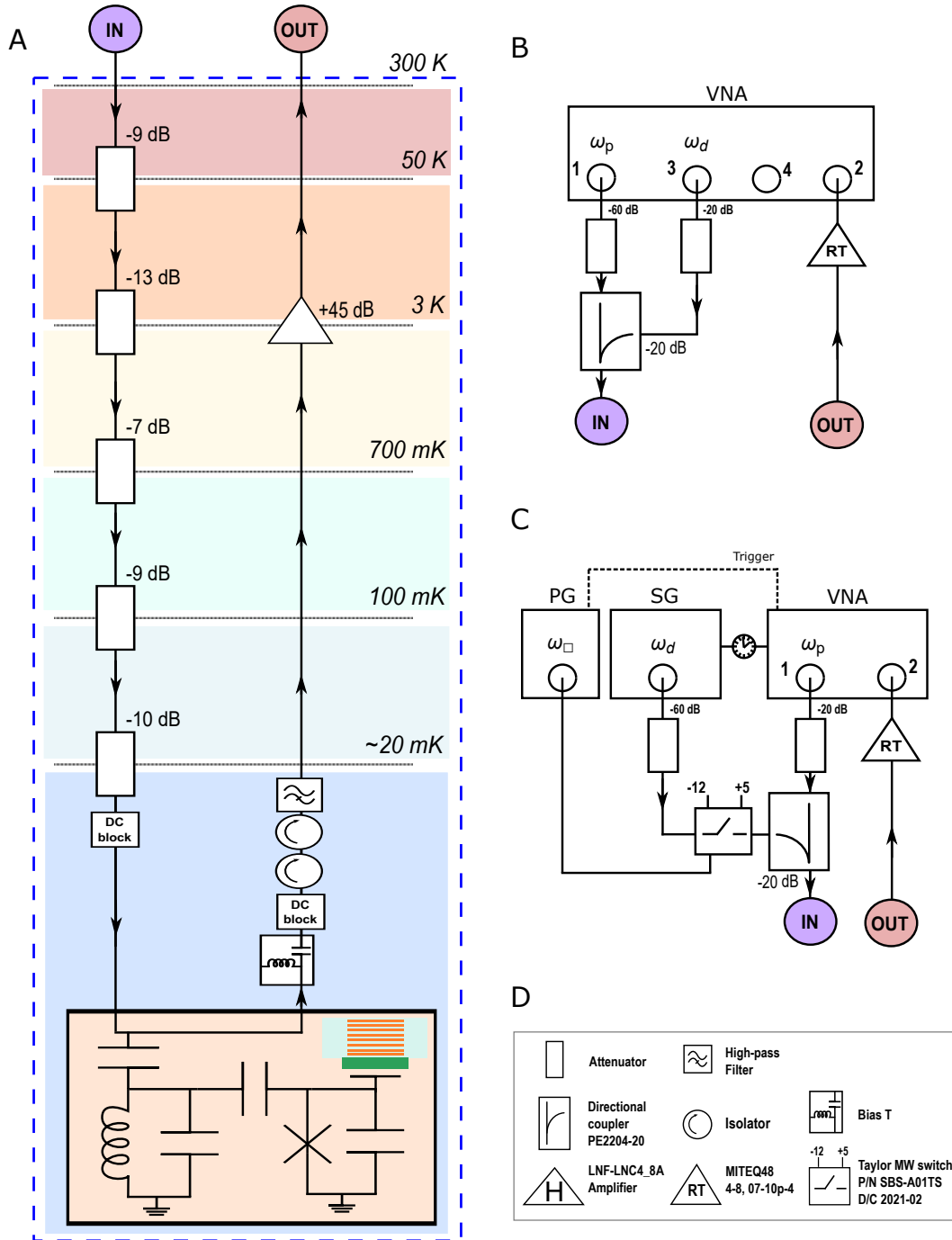


FIG. S2. **Schematic of the measurement setup.** To the left is the general Dilution refrigerator wiring setup. Outside the refrigerator, we used two different setups. In (b), we show our Two-tone spectroscopy configuration used for qubit spectroscopy. Here, we sent a weak continuous wave tone (readout resonator probe) from the vector network analyzer (VNA) port one and a second continuous wave tone (qubit drive) from the VNA port 3. These two signals are combined by using a directional coupler before entering the dilution refrigerator. The signal from the dilution refrigerator goes through a room-temperature amplifier before it goes to port 2 of the VNA. In (c), we show are "time domain" setup. Here, we replaced output port 3 of the VNA with a signal generator (SG) to provide the drive tone. A switch (*Taylor MW switch*) together with a pulse generator (PG, *Rigol DG1022*) is placed between the directional coupler and the signal generator.

frequency ω_d , which we call the drive tone. The experiment measures the coupling between the qubit and the phonon mode via two-tone spectroscopy performed via the cavity. The procedure consists of considering the cavity detuned from the qubit, setting the probe tone at the (shifted) cavity frequency and varying the drive tone close to the qubit Lamb-shifted frequency. The transmission of the cavity carries information about the qubit correlations $\langle \hat{\sigma}_z \rangle$. The phonon mode has a frequency close to the qubit frequency.

We model the system with the Hamiltonian

$$\begin{aligned} \frac{\hat{\mathcal{H}}}{\hbar} = & \omega_r \hat{a}^\dagger \hat{a} + \omega_b \hat{b}^\dagger \hat{b} + \frac{\omega_q}{2} \hat{\sigma}_z + g_{qc} (\hat{a} \hat{\sigma}_+ + \hat{a}^\dagger \hat{\sigma}_-) + g_{qb} (\hat{b}^\dagger \hat{\sigma}_- + \hat{b} \hat{\sigma}_+) \\ & + \epsilon_d (\hat{a} e^{i\omega_d t} + \hat{a}^\dagger e^{-i\omega_d t}) + \epsilon_p (\hat{a} e^{i\omega_p t} + \hat{a}^\dagger e^{-i\omega_p t}), \end{aligned} \quad (\text{S1})$$

where $\hat{a}^{(\dagger)}$ are the annihilation (creation) operators for the readout cavity with frequency ω_r , $\hat{b}^{(\dagger)}$ are the annihilation (creation) operators for the HBAR mode with frequency ω_b , $\hat{\sigma}_z$ is the qubit population operator with qubit frequency ω_q . The couplings are defined by the rates g_{qc} between the qubit and the readout cavity and g_{qb} between the qubit and the HBAR mode, where we assume that $g_{qc} \gg g_{qb}$. Finally, the two drives are described by the amplitude $\epsilon_{p,d}$ with frequencies $\omega_{p,d}$. The system is operated in the cavity-qubit dispersive regime $g_{qc} \ll |\omega_r - \omega_q|$. We then consider the standard Schrieffer-Wolff transformation up to the first order in $g_{qc}/|\omega_r - \omega_q|$. Defining $\chi = g_{qc}^2/(\omega_q - \omega_r)$, the transformed Hamiltonian reads

$$\begin{aligned} \frac{\hat{\mathcal{H}}'}{\hbar} = & \frac{\tilde{\Omega}_q}{2} \hat{\sigma}_z + \omega_r \hat{a}^\dagger \hat{a} + \omega_b \hat{b}^\dagger \hat{b} + \chi \hat{a}^\dagger \hat{a} \hat{\sigma}_z + g_{qb} (\hat{b}^\dagger \hat{\sigma}_- + \hat{b} \hat{\sigma}_+) - \frac{g_{qb}}{g_{qc}} \chi (\hat{a}^\dagger \hat{b} + \hat{a} \hat{b}^\dagger) \hat{\sigma}_z \\ & + \sum_{j=p,d} \epsilon_j (\hat{a} e^{i\omega_j t} + \hat{a}^\dagger e^{-i\omega_j t}) + \frac{g_{qc}}{\omega_r - \omega_q} \sum_{j=p,d} \epsilon_j (\hat{\sigma}_+ e^{i\omega_j t} + \hat{\sigma}_- e^{-i\omega_j t}). \end{aligned} \quad (\text{S2})$$

The Lamb-shifted qubit frequency is $\tilde{\Omega}_q = \omega_q + \chi$. Given the system's parameters, we will discard the qubit-mediated beam-splitter term $\frac{g_{qb}}{g_{qc}} \chi (\hat{a}^\dagger \hat{b} + \hat{a} \hat{b}^\dagger) \hat{\sigma}_z$. Furthermore, in the two-tone spectroscopic setup, we can retain only the probe term for the cavity and only the drive term for the qubit. With such approximations, we have

$$\begin{aligned} \frac{\hat{\mathcal{H}}'}{\hbar} = & \frac{\tilde{\Omega}_q}{2} \hat{\sigma}_z + \omega_r \hat{a}^\dagger \hat{a} + \omega_b \hat{b}^\dagger \hat{b} + \chi \hat{a}^\dagger \hat{a} \hat{\sigma}_z + g_{qb} (\hat{b}^\dagger \hat{\sigma}_- + \hat{b} \hat{\sigma}_+) \\ & + \epsilon_p (\hat{a} e^{i\omega_p t} + \hat{a}^\dagger e^{-i\omega_p t}) + \epsilon_d (\hat{\sigma}_+ e^{i\omega_d t} + \hat{\sigma}_- e^{-i\omega_d t}), \end{aligned} \quad (\text{S3})$$

where we have defined $\epsilon_d = \frac{g_{qc}\epsilon_d}{\omega_q - \omega_r}$. It is convenient to move to a frame co-rotating with the pump and the probe frequencies, for which the Hamiltonian in Eq. (S3) reads

$$\begin{aligned} \frac{\hat{\mathcal{H}}'_{\text{rot}}}{\hbar} = & -\frac{\Delta_q}{2} \hat{\sigma}_z + (-\Delta_r + \chi) \hat{a}^\dagger \hat{a} - \Delta_b \hat{b}^\dagger \hat{b} + \chi \hat{a}^\dagger \hat{a} \hat{\sigma}_z \\ & + g_{qb} (\hat{b}^\dagger \hat{\sigma}_- + \hat{b} \hat{\sigma}_+) + \epsilon_p (\hat{a} + \hat{a}^\dagger) + \epsilon_d (\hat{\sigma}_+ + \hat{\sigma}_-), \end{aligned} \quad (\text{S4})$$

where $\Delta_b = \omega_d - \omega_b$, $\Delta_q = \omega_d - \tilde{\Omega}_q$, and $\Delta_r = \omega_p - \omega_r + \chi$. We have defined the readout cavity detuning Δ_r to included the Lamb shift, however, this decision is arbitrary. The density matrix of the system ρ has dynamics described by the master equation

$$\partial_t \rho = -\frac{i}{\hbar} [\hat{\mathcal{H}}'_{\text{rot}}, \rho] + \kappa \mathcal{L}[\hat{a}] \rho + \gamma_b \mathcal{L}[\hat{b}] \rho + \Gamma_1 \mathcal{L}[\hat{\sigma}_-] \rho + \frac{\Gamma_\phi}{2} \mathcal{L}[\hat{\sigma}_z] \rho. \quad (\text{S5})$$

Here κ is the cavity decay, γ_b is the phonon decay, Γ_1 is the qubit population decay, and Γ_ϕ is the qubit dephasing. We have assumed zero temperature and ignored small corrections to the dissipator due to the Schrieffer-Wolff transformation.

B. Qubit Two-Tone Spectroscopy

Following the arguments presented in⁴⁶, ignoring the qubit-phonon coupling, in the dispersive regime, $\arg[\langle \hat{a}(t) \rangle]$ is directly related to the qubit population $\langle \hat{\sigma}_z(t) \rangle$. By recording the phase of the readout resonator, one can then obtain the qubit absorption spectrum

$$S(\omega) = \frac{1}{2\pi} \int_{-\infty}^{\infty} dt e^{i\omega t} \langle \hat{\sigma}_-(t) \hat{\sigma}_+(0) \rangle_s, \quad (\text{S6})$$

where $\langle \cdot \rangle_s$ indicates that the expectation value is taken in the steady state.

It was shown that for a qubit-cavity system, the qubit absorption spectrum is given by⁴⁶

$$S(\omega) = \frac{1}{\pi} \sum_{j=0}^{\infty} \frac{1}{j!} \operatorname{Re} \left(\frac{(-A)^j e^A}{\Gamma_q^{(j)}/2 - i(\omega - \Omega_q^{(j)})} \right) \equiv \sum_{j=0}^{\infty} S_j(\omega), \quad (\text{S7})$$

with

$$\begin{aligned} A &= D_{ss} \left(\frac{\kappa/2 - 2i\chi}{\kappa/2 + 2i\chi} \right), \\ B &= \chi(\bar{n}_e + \bar{n}_g - D_{ss}), \\ D_{ss} &= \frac{2\chi^2(\bar{n}_e + \bar{n}_g)}{(\kappa/2)^2 + 2\chi^2}, \\ \bar{n}_e &= \frac{\bar{n}_g(\kappa/2)^2}{(\kappa/2)^2 + (2\chi)^2}, \\ \Gamma_q^{(j)} &= 2\gamma_q + \kappa(j + D_{ss}), \\ \omega_q^{(j)} &= \tilde{\omega}_q + B + 2j\chi. \end{aligned} \quad (\text{S8})$$

In the above equations, $\omega_q^{(j)}$ and $\Gamma_q^{(j)}$ are the frequency and linewidth of the qubit with the readout resonator in the state $|j\rangle$, respectively. The intrinsic qubit linewidth, with the readout resonator in its ground state, is given by $\gamma_q = \Gamma_1/2 + \Gamma_\phi$, where Γ_1 is the longitudinal relaxation rate, and Γ_ϕ is the pure dephasing rate. The qubit frequency $\omega_q^{(0)}$ is ac Stark shifted by B from its intrinsic value ω_q . We have also assumed that the readout drive is on resonance with the readout resonator, i.e. $\Delta_r = 0$, and the readout resonator has a full-width half-maximum linewidth κ . In the limit $\chi \sim \kappa$ and with $\Delta_r = 0$, the components $S_j(\omega)$ have non-Lorentzian lineshapes and can even be negative. The sum of these individual components can result in an asymmetry of the qubit spectrum, as seen in Fig. S3(a).

We perform spectroscopy of the qubit by monitoring the transmission coefficient S_{21} of the readout resonator as a function of the qubit drive frequency ω_d . The probe tone was fixed at the Stark-shifted readout resonator frequency with the qubit in its ground state $\omega_c^g/2\pi = 4.91$ GHz, such that $\Delta_r = 0$ and held at a constant power $\mathcal{P}_d = -25$ dBm, set at room temperature. The probe line has a total of 108 dB of attenuation, ensuring the average number of photons in the probe mode on average is much less than one.

To fit the measured spectrum, we use the expression,

$$|S_{21}| = \mathcal{A} \sum_{j=0}^{10} S_j(\omega) + \mathcal{C}, \quad (\text{S9})$$

where \mathcal{A} is a conversion factor between $S_j(\omega)$ and $|S_{21}|$ and \mathcal{C} is a constant offset of the spectrum. The value of the Fock basis was truncated to $j = 10$, and the linewidth of the readout resonator was independently determined and fixed; see Table. I. The fitting parameters include the intrinsic qubit frequency ω_q , the power broadened qubit linewidth $\Gamma_q(\mathcal{P}_d)$, where \mathcal{P}_d is the qubit drive power, the qubit dispersive shift χ , the probe mode occupancy with the qubit in its ground state \bar{n}_g , and conversion factor \mathcal{A} , and the constant offset \mathcal{C} .

An example spectrum and its fit are shown in Fig. S3(a). First, the value of the dispersive shift was determined to be $\chi = -1.2 \pm 0.2$ MHz, which agreed with our designed value. This value was then fixed, and the data was fit for all qubit drive powers to determine the remaining values. We found that the ground state readout photon population depended on the qubit drive power. This is likely due to the heating of the silicon substrate because the qubit drive tone was applied via the readout resonator. The value of $\bar{n}_g(\mathcal{P}_d)$ is shown in Fig. S3(b). The zero power qubit linewidth was also extracted by extrapolating the measured power-broadened qubit linewidth to zero power and was determined to be $\gamma_q(0) = 0.420 \pm 0.04$ MHz, which agrees with our $\gamma_q = \Gamma_1/2 + \Gamma_\phi \geq 1/2T_1$ limit determined using a time-domain measurement with $T_1 = 180 \pm 30$ ns. The comparison between our spectroscopy and time domain measurements indicates that our qubit decay is dominated by decoherence, and therefore we have ignored intrinsic dephasing in our model since qubit dephasing will be dominated by power-induced dephasing induced by the qubit drive tone.

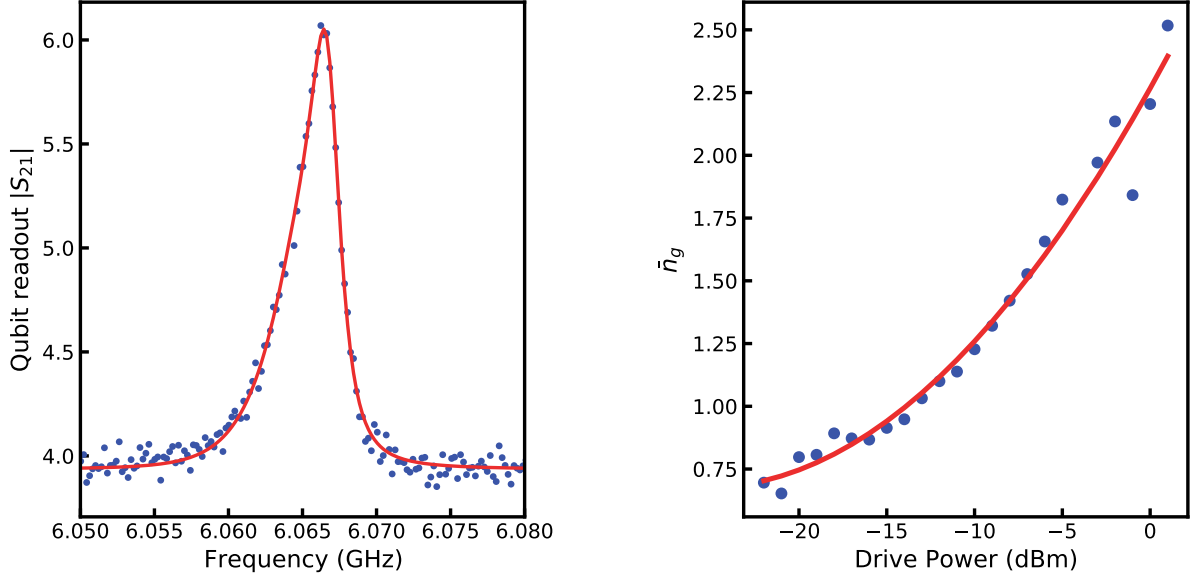


FIG. S3. **Two-tone qubit spectroscopy measurements.** (A) Experimental two-tone qubit spectrum (blue) and the qubit spectrum determined from a fit to Eq. S9 (red). The qubit drive power at room temperature was set to -20.0 dBm. (B) Extracted value of the readout resonator photon population as a function of qubit drive power.

C. Master Equation Simulations

Qubit Spectroscopy

We simulate the dynamics of the master equation Eq. S5 using the Python package Qutip⁵². We first compare the measured qubit spectrum without the phonon mode to the Qutip steady-state simulations. To begin, we must consider the non-zero photon population of the readout resonator. The finite population results in an asymmetry in the qubit spectrum, as well as additional measurement-induced dephasing. To include the finite readout population in our simulation, the readout drive ϵ_p was set such that the average population $\langle \hat{a}^\dagger \hat{a} \rangle = \bar{n}_g(\mathcal{P}_d)$. This ensured that for each qubit drive power, the readout resonator had the appropriate number of steady-state photons.

To account for qubit power-broadening, the qubit drive power in the simulation had to be calibrated. As stated above, $\epsilon_d = \frac{g_{qc}\epsilon_d}{\omega_r - \Omega_q}$, where $\epsilon_d = \sqrt{\kappa_{\text{ext}} \sqrt{\mathcal{P}_d} / \hbar \omega_d}$, κ_{ext} is the external coupling rate to the readout resonator, and \mathcal{P}_d is the drive power in Watts at the coupling port of the readout resonator. Therefore, the drive coefficient ϵ_d can be written in the form

$$\epsilon_d = \sqrt{10(\mathcal{P}_{\text{RT}} + \delta)/10} \quad (\text{S10})$$

where δ calibrates the room-temperature power to the corresponding value of \mathcal{P}_d accounting for all losses and multiplicative factors. The value of δ was determined by matching the simulation to the power-broadened qubit spectrum at multiple qubit drive powers. A set of qubit spectra is shown in Fig. S4 where it can be seen that the master equation simulation is in excellent agreement capturing the qubit asymmetry at low power, and the power-broadened qubit spectrum at higher drive powers. It should be noted the measured transmission signal S_{21} is proportional to the qubit population $\langle \hat{\sigma}_z \rangle$ only if the appropriate signal quadrature is measured. Here this was determined by calculating the rotation angle that minimized the signal in the out-of-phase quadrature. To confirm, we compared our single-trace two-tone data with a direct measurement of the readout resonator frequency at several qubit drive powers. At the highest drive powers, we observed a slight deviation resulting from signal mixing into the out-of-phase quadrature. However, this was at the drive powers above the self-quenching threshold and resulted in a slight mismatch between our experimental and simulated two-tone traces.

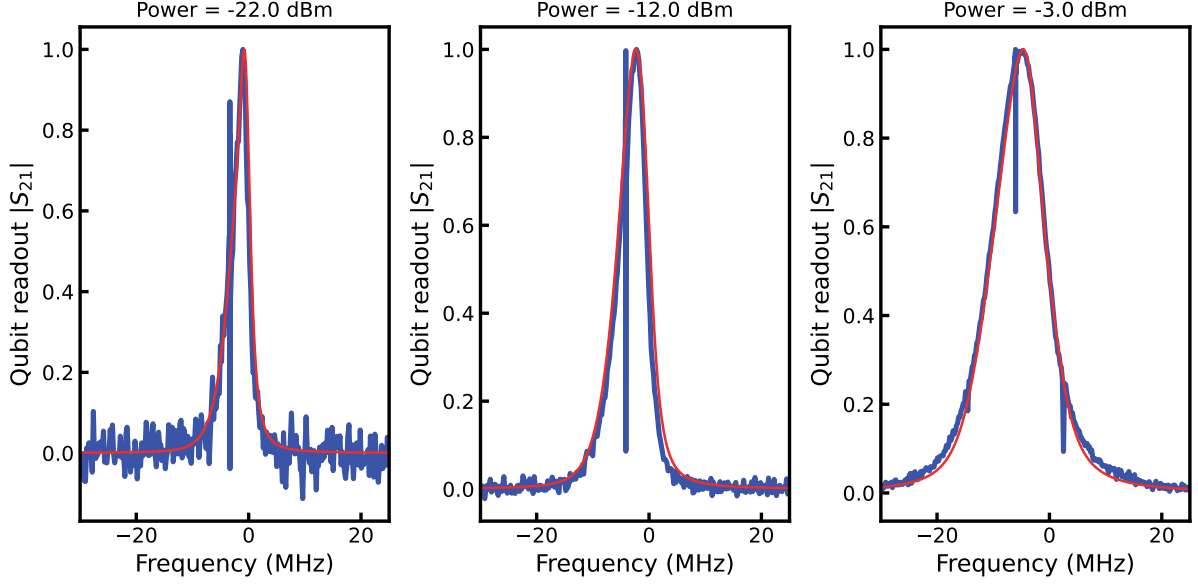


FIG. S4. **Two-tone qubit spectroscopy measurements.** (A) Experimental two-tone qubit spectrum (blue) overlapped with the qubit spectrum determined from the master equation simulation (red). The frequency is defined as the detuning from the bare qubit frequency. The qubit drive power at room temperature was set to -12.0 dBm. (B) Qubit spectrum and master equation simulation for a qubit drive power of -6.0 dBm. (C) Qubit spectrum and master equation simulation for a qubit drive power of -3.0 dBm. The feature at ~ 0 MHz is an additional HBAR mode, one free-spectral range from the HBAR mode of interest for this work. The only parameter that was varied within the simulation was the room-temperature value of the qubit drive.

Gated Ringdown

Following the calibration of the qubit spectrum, the phonon mode was included in the master equation simulation. The value of the coupling rate g_{qb} and the phonon linewidth γ_b were determined by performing a fit to the time domain gated two-tone measurements. The fit was determined by fitting both the ringdown (as shown in the main text) and also the ring-up of the qubit. The best-fit values were then compared at multiple drive powers; see Fig. S5(a). We extracted a value of the qubit phonon coupling of $g_{qb}/2\pi = 162$ kHz and a phonon linewidth of $\gamma_b/2\pi = 6.81$ kHz. From this set of simulations, the steady-state phonon population and phonon statistics can be estimated for multiple drive powers. We observe a good agreement between the numerical simulation and the ring-up data and an excellent agreement between the ringdown data for all powers. Deviations in the ring-up simulations likely result from higher-order nonlinearities we are not considering in our model.

The master equation simulations directly calculate the time dynamics of $\langle \hat{\sigma}_+ \hat{\sigma}_- \rangle$, this value has been scaled by the same constant factor for all powers to give a direct comparison to our two-tone measurement. Since we expect the variation in the transmission coefficient measured in the two-tone measurement to be proportional to $\langle \hat{\sigma}_+ \hat{\sigma}_- \rangle$, see Eq. S3 and Ref. ⁴⁶. From our simulation, we calculate the phonon population and second-order correlation function for multiple drive powers, shown in Fig. S5(b,c). For low drive powers, the phonon statistics are described by a coherent state, $g^{(2)}(0) \approx 1.0$, as expected for a laser. However, as discussed in the main text, single-atom lasers exhibit self-quenching above a given upper-threshold power. This can be seen in both the phonon population, as a rapid decrease in the populations, and in the phonon statistics as $g^{(2)}(0) > 1.0$ for drive powers above the self-quenching threshold.

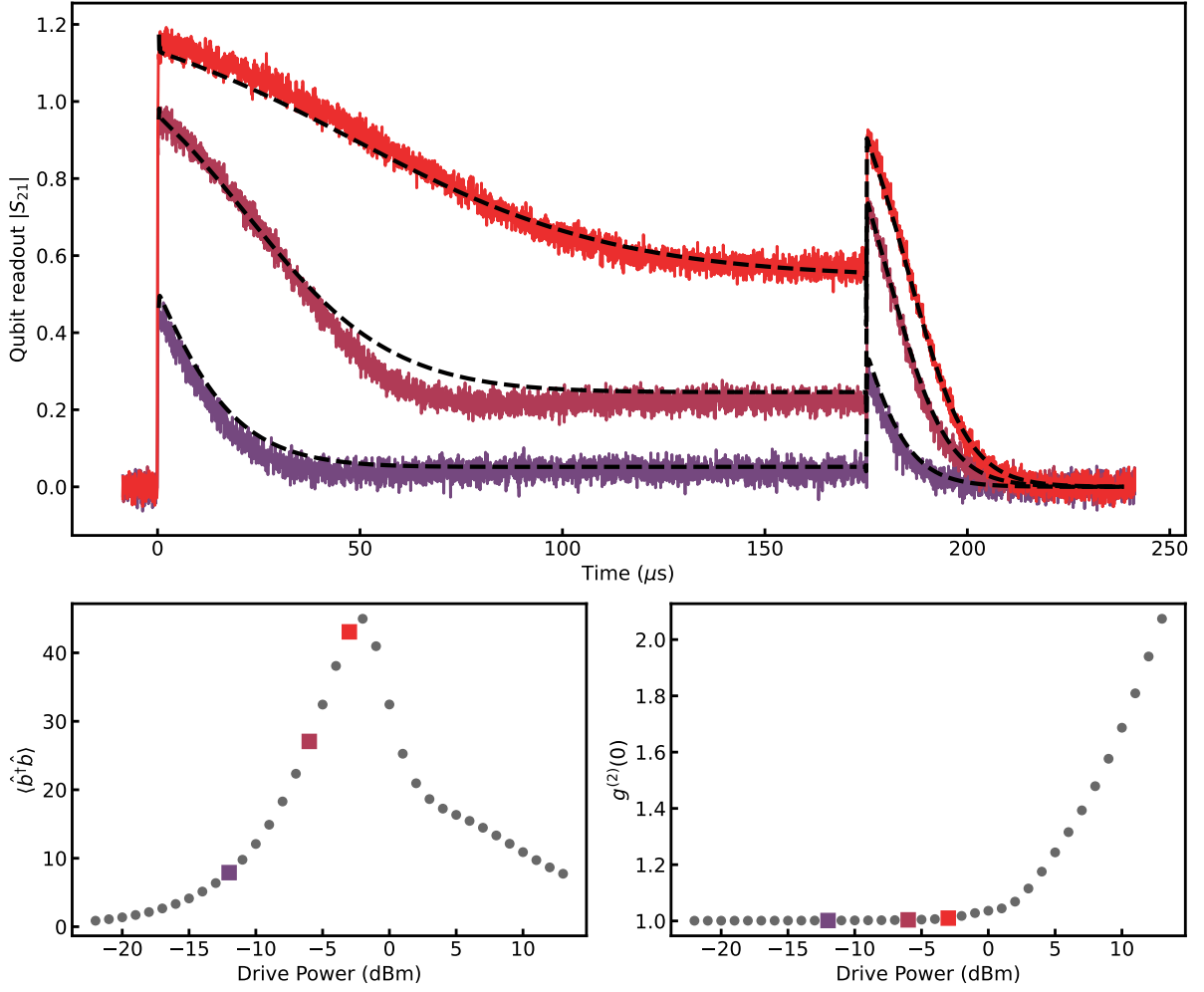


FIG. S5. **Gated two-tone qubit spectroscopy.** (A) Experimental gated two-tone measurements for qubit drive powers -12.0, -6.0, -3.0 dBm. The master equation simulations at the same drive power are plotted as dashed black lines. The simulation has an excellent agreement for the ringdown data for all powers and a slight deviation from the ring-up data. This could be attributed to higher-order non-linearities we are not considering within our simple master equation model. However, the agreement between the experiment and simulation is good for all powers. (B) Simulated phonon state population $\langle \hat{b}^\dagger \hat{b} \rangle$ as a function of qubit drive power. (C) Simulated second-order phonon correlations $g^{(2)}(0)$ as a function of qubit drive power.

TABLE I. Symbols and parameters

Parameter	Symbol
Microwave mode frequency	$\omega_c = 2\pi \times 4.910$ GHz
Microwave mode decay	$\kappa = 2\pi \times 2.897$ MHz
Phonon mode frequency	$\omega_b = 2\pi \times 6.064$ GHz
Phonon mode decay	$\gamma_b = 2\pi \times 6.81$ kHz
Qubit frequency	$\Omega_q = 2\pi \times 6.067$ GHz
Qubit energy relaxation rate	$\Gamma_1 = 2\pi \times 0.840$ MHz
Qubit phase relaxation rate	$\Gamma_\phi < 2\pi \times 0.08$ MHz
Qubit-phonon coupling	$g_{qb} = 2\pi \times 162$ kHz
Dispersive cavity-qubit coupling	$\chi = -2\pi \times 1.2$ MHz
Lamb-shifted qubit frequency	$\tilde{\Omega}_q = \Omega_q - \chi$
Qubit drive frequency	ω_d , varied around Ω_q
Cavity probe frequency	ω_p , set at the Stark-shifted cavity frequency

- ¹A. L. Schawlow, "Spectroscopy in a new light," *Reviews of Modern Physics* **54**, 697 (1982).
- ²A. L. Schawlow, "Laser spectroscopy of atoms and molecules: The abundance of new laser techniques is making possible a variety of spectroscopic experiments." *Science* **202**, 141–147 (1978).
- ³W. D. Phillips and H. Metcalf, "Laser deceleration of an atomic beam," *Physical Review Letters* **48**, 596 (1982).
- ⁴W. D. Phillips, "Nobel lecture: Laser cooling and trapping of neutral atoms," *Reviews of Modern Physics* **70**, 721 (1998).
- ⁵M. H. Anderson, J. R. Ensher, M. R. Matthews, C. E. Wieman, and E. A. Cornell, "Observation of bose-einstein condensation in a dilute atomic vapor," *science* **269**, 198–201 (1995).
- ⁶K. B. Davis, M.-O. Mewes, M. R. Andrews, N. J. van Druten, D. S. Durfee, D. Kurn, and W. Ketterle, "Bose-einstein condensation in a gas of sodium atoms," *Physical review letters* **75**, 3969 (1995).
- ⁷B. P. Abbott, R. Abbott, T. Abbott, M. Abernathy, F. Acernese, K. Ackley, C. Adams, T. Adams, P. Addesso, R. Adhikari, *et al.*, "Observation of gravitational waves from a binary black hole merger," *Physical review letters* **116**, 061102 (2016).
- ⁸S. Chaurasiya, P. Hew, P. Crosley, D. Sharon, K. Potts, K. Agopsowicz, M. Long, C. Shi, and M. Hitt, "Breast cancer gene therapy using an adenovirus encoding human il-2 under control of mammaglobin promoter/enhancer sequences," *Cancer Gene Therapy* **23**, 178–187 (2016).
- ⁹R. L. McCreery, *Raman spectroscopy for chemical analysis* (John Wiley & Sons, 2005).
- ¹⁰E. Khalkhal, M. Rezaei-Tavirani, M. R. Zali, and Z. Akbari, "The evaluation of laser application in surgery: a review article," *Journal of lasers in medical sciences* **10**, S104 (2019).
- ¹¹I. Mahboob, K. Nishiguchi, A. Fujiwara, and H. Yamaguchi, "Phonon lasing in an electromechanical resonator," *Phys. Rev. Lett.* **110**, 127202 (2013).
- ¹²K. Vahala, M. Herrmann, S. Knünz, V. Batteiger, G. Saathoff, T. Hänsch, and T. Udem, "A phonon laser," *Nature Physics* **5**, 682–686 (2009).
- ¹³R. M. Pettit, W. Ge, P. Kumar, D. R. Luntz-Martin, J. T. Schultz, L. P. Neukirch, M. Bhattacharya, and A. N. Vamivakas, "An optical tweezer phonon laser," *Nature Photonics* **13**, 402–405 (2019).
- ¹⁴T. Kuang, R. Huang, W. Xiong, Y. Zuo, X. Han, F. Nori, C.-W. Qiu, H. Luo, H. Jing, and G. Xiao, "Nonlinear multi-frequency phonon lasers with active levitated optomechanics," *Nature Physics* **19**, 414–419 (2023).
- ¹⁵T. Behrle, T. L. Nguyen, F. Reiter, D. Baur, B. de Neeve, M. Stadler, M. Marinelli, F. Lancellotti, S. F. Yelin, and J. P. Home, "Phonon laser in the quantum regime," *Phys. Rev. Lett.* **131**, 043605 (2023).
- ¹⁶P. K. Shandilya, D. P. Lake, M. J. Mitchell, D. D. Sukachev, and P. E. Barclay, "Optomechanical interface between telecom photons and spin quantum memory," *Nature Physics* **17**, 1420–1425 (2021).
- ¹⁷D. Hatanaka, M. Asano, H. Okamoto, Y. Kunihashi, H. Sanada, and H. Yamaguchi, "On-chip coherent transduction between magnons and acoustic phonons in cavity magnomechanics," *Physical Review Applied* **17**, 034024 (2022).
- ¹⁸D. Hatanaka, M. Asano, H. Okamoto, and H. Yamaguchi, "Phononic crystal cavity magnomechanics," *Physical Review Applied* **19**, 054071 (2023).
- ¹⁹K. Cui, Z. Huang, N. Wu, Q. Xu, F. Pan, J. Xiong, X. Feng, F. Liu, W. Zhang, and Y. Huang, "Phonon lasing in a hetero optomechanical crystal cavity," *Photonics Research* **9**, 937–943 (2021).
- ²⁰J. Zhang, B. Peng, Ş. K. Özdemir, K. Pichler, D. O. Krimer, G. Zhao, F. Nori, Y.-x. Liu, S. Rotter, and L. Yang, "A phonon laser operating at an exceptional point," *Nature Photonics* **12**, 479–484 (2018).
- ²¹I. S. Grudinin, H. Lee, O. Painter, and K. J. Vahala, "Phonon laser action in a tunable two-level system," *Phys. Rev. Lett.* **104**, 083901 (2010).
- ²²C. A. Potts, E. Varga, V. A. S. V. Bittencourt, S. Viola-Kusminskiy, and J. P. Davis, "Dynamical backaction magnomechanics," *Physical Review X* **11**, 031053 (2021).
- ²³P. Parsa, P. K. Shandilya, D. P. Lake, M. E. Mitchell, and P. E. Barclay, "Feedback enhanced phonon lasing of a microwave frequency resonator," *arXiv preprint arXiv:2308.09130* (2023).
- ²⁴T. J. Kippenberg and K. J. Vahala, "Cavity optomechanics: back-action at the mesoscale," *science* **321**, 1172–1176 (2008).
- ²⁵W. Bron and W. Grill, "Stimulated phonon emission," *Physical Review Letters* **40**, 1459 (1978).
- ²⁶S. Wallentowitz, W. Vogel, I. Siemers, and P. Toschek, "Vibrational amplification by stimulated emission of radiation," *Physical Review A* **54**, 943 (1996).
- ²⁷I. Camps, S. Makler, H. Pastawski, and L. F. Torres, "Gaas-al x ga l- x as double-barrier heterostructure phonon laser: A full quantum treatment," *Physical Review B* **64**, 125311 (2001).
- ²⁸J. McKeever, A. Boca, A. D. Boozer, J. R. Buck, and H. J. Kimble, "Experimental realization of a one-atom laser in the regime of strong coupling," *Nature* **425**, 268–271 (2003).
- ²⁹F. Dubin, C. Russo, H. G. Barros, A. Stute, C. Becher, P. O. Schmidt, and R. Blatt, "Quantum to classical transition in a single-ion laser," *Nature Physics* **6**, 350–353 (2010).
- ³⁰K. An, J. J. Childs, R. R. Dasari, and M. S. Feld, "Microlaser: A laser with one atom in an optical resonator," *Physical review letters* **73**, 3375 (1994).
- ³¹Y. Mu and C. Savage, "One-atom lasers," *Physical Review A* **46**, 5944 (1992).
- ³²S. Ashhab, J. Johansson, A. Zagoskin, and F. Nori, "Single-artificial-atom lasing using a voltage-biased superconducting charge qubit," *New Journal of Physics* **11**, 023030 (2009).
- ³³M. Bild, M. Fadel, Y. Yang, U. von Lüpke, P. Martin, A. Bruno, and Y. Chu, "Schrödinger cat states of a 16-microgram mechanical oscillator," *Science* **380**, 274–278 (2023).
- ³⁴M. F. Gely and G. A. Steele, "Superconducting electro-mechanics to test diósi-penrose effects of general relativity in massive superpositions," *AVS Quantum Science* **3**, 035601 (2021).
- ³⁵B. Schriniski, Y. Yang, U. von Lüpke, M. Bild, Y. Chu, K. Hornberger, S. Nimmrichter, and M. Fadel, "Macroscopic quantum test with bulk acoustic wave resonators," *Phys. Rev. Lett.* **130**, 133604 (2023).
- ³⁶M. Wybourne and J. Wigmore, "Phonon spectroscopy," *Reports on Progress in Physics* **51**, 923 (1988).
- ³⁷O. Romero-Isart, A. C. Pflanzer, F. Blaser, R. Kaltenbaek, N. Kiesel, M. Aspelmeyer, and J. I. Cirac, "Large quantum superpositions and interference of massive nanometer-sized objects," *Phys. Rev. Lett.* **107**, 020405 (2011).
- ³⁸U. von Lüpke, I. C. Rodrigues, Y. Yang, M. Fadel, and Y. Chu, "Engineering phonon-phonon interactions in multimode circuit quantum acousto-dynamics," *arXiv preprint arXiv:2303.00730* (2023).
- ³⁹U. von Lüpke, Y. Yang, M. Bild, L. Michaud, M. Fadel, and Y. Chu, "Parity measurement in the strong dispersive regime of circuit

- quantum acoustodynamics,” *Nature Physics* **18**, 794–799 (2022).
- ⁴⁰Y. Chu, P. Kharel, T. Yoon, L. Frunzio, P. T. Rakich, and R. J. Schoelkopf, “Creation and control of multi-phonon fock states in a bulk acoustic-wave resonator,” *Nature* **563**, 666–670 (2018).
- ⁴¹Y. Chu, P. Kharel, W. H. Renninger, L. D. Burkhardt, L. Frunzio, P. T. Rakich, and R. J. Schoelkopf, “Quantum acoustics with superconducting qubits,” *Science* **358**, 199–202 (2017).
- ⁴²A. Vålímaa, W. Crump, M. Kervinen, and M. A. Sillanpää, “Multiphonon transitions in a quantum electromechanical system,” *Phys. Rev. Appl.* **17**, 064003 (2022).
- ⁴³W. Crump, A. Vålímaa, and M. A. Sillanpää, “Coupling high-overtone bulk acoustic wave resonators via superconducting qubits,” *arXiv preprint arXiv:2307.05544* (2023).
- ⁴⁴P. Krantz, M. Kjaergaard, F. Yan, T. P. Orlando, S. Gustavsson, and W. D. Oliver, “A quantum engineer’s guide to superconducting qubits,” *Applied physics reviews* **6** (2019).
- ⁴⁵M. Reed, L. DiCarlo, B. Johnson, L. Sun, D. Schuster, L. Frunzio, and R. Schoelkopf, “High-fidelity readout in circuit quantum electrodynamics using the jaynes-cummings nonlinearity,” *Physical review letters* **105**, 173601 (2010).
- ⁴⁶J. Gambetta, A. Blais, D. I. Schuster, A. Wallraff, L. Frunzio, J. Majer, M. H. Devoret, S. M. Girvin, and R. J. Schoelkopf, “Qubit-photon interactions in a cavity: Measurement-induced dephasing and number splitting,” *Physical Review A* **74**, 042318 (2006).
- ⁴⁷D. Lachance-Quirion, Y. Tabuchi, S. Ishino, A. Noguchi, T. Ishikawa, R. Yamazaki, and Y. Nakamura, “Resolving quanta of collective spin excitations in a millimeter-sized ferromagnet,” *Science Advances* **3**, e1603150 (2017).
- ⁴⁸D. Schuster, A. Wallraff, A. Blais, L. Frunzio, R.-S. Huang, J. Majer, S. Girvin, and R. J. Schoelkopf, “ac stark shift and dephasing of a superconducting qubit strongly coupled to a cavity field,” *Physical Review Letters* **94**, 123602 (2005).
- ⁴⁹J. P. Gordon, H. J. Zeiger, and C. H. Townes, “The maser-new type of microwave amplifier, frequency standard, and spectrometer,” *Physical review* **99**, 1264 (1955).
- ⁵⁰“Scixel,” <https://scixel.es/>, accessed: 2023-09-28.
- ⁵¹D. J. Thoen, B. G. C. Bos, E. Haalebos, T. Klapwijk, J. Baselmans, and A. Endo, “Superconducting nbtin thin films with highly uniform properties over a 100 mm wafer,” *IEEE Transactions on Applied Superconductivity* **27**, 1–5 (2016).
- ⁵²J. R. Johansson, P. D. Nation, and F. Nori, “Qutip: An open-source python framework for the dynamics of open quantum systems,” *Computer Physics Communications* **183**, 1760–1772 (2012)